International Journal of Heat and Mass Transfer 52 (2009) 3665–3675

Contents lists available at ScienceDirect

International Journal of Heat and Mass Transfer

journal homepage: www.elsevier.com/locate/ijhmt

Liquid film dryout in a boiling channel under flow oscillation conditions

Tomio Okawa *, Taisuke Goto, Jun Minamitani, Yosuke Yamagoe

Department of Mechanical Engineering, Osaka University 2-1, Yamadaoka, Suita-shi, Osaka 565-0871, Japan

ARTICLE INFO

Article history:
Received 2 July 2008
Received in revised form 26 November 2008
Accepted 27 February 2009
Available online 7 April 2009

Keywords:
Flow boiling
Critical heat flux
Flow oscillation
Annular two-phase flow
Liquid film dryout

ABSTRACT

A simple theory was developed to elucidate the influence of sinusoidal oscillation of the inlet flow rate on the occurrence of liquid film dryout in an annular two-phase flow regime in a boiling channel. The theory assumes that the critical heat flux (CHF) under an oscillatory condition can be calculated from values in steady states provided that the effect of axial mixing of the liquid film is appropriately considered. The trends of CHFs calculated using a one-dimensional three-fluid model and those experimentally measured under atmospheric pressure were in reasonable agreement with the proposed theory. However, the CHF values measured under oscillatory conditions were usually higher in the experiment than in the numerical simulation, which indicated that axial liquid transport induced by disturbance waves might enhance axial mixing of the liquid film.

1. Introduction

In the design of advanced boiling water reactors, a core with high power density is frequently adopted to further enhance economic efficiency [1–4]. In industrial plants that use a forced convective boiling heat transfer, however, increased power density generally leads to the reduction of the margin to the onset of unanticipated flow instability. Hence, to ensure the safety of plants with high power density, it is necessary to predict the occurrence of boiling transition even when the coolant flow rate becomes oscillatory.

Flow instability is one of the fundamentally important issues of boiling two-phase flow systems including boilers and nuclear reactors, particularly during transient situations such as startup and partial-load operation. Accordingly, many experimental studies have been carried out to clarify the effects of flow instability on critical heat flux in a boiling channel as reviewed extensively by Ozawa et al. [5]. It was found that destabilization of the flow rate results in a noticeable decrease in the critical heat flux. However, in the experiments performed under unstable conditions, it is difficult to systematically investigate the effects of the amplitude and frequency of flow oscillation since these parameters are largely dependent on the geometries of the experimental apparatus. Ozawa et al. [6] and Umekawa et al. [7] therefore imposed forced oscillation on the inlet flow rate, enabling almost-arbitrary control of the amplitude and frequency. It was shown clearly in these experiments that an increase in the amplitude and a decrease in the frequency lead to a reduction in the critical heat flux.

The main objective of this work is to elucidate the mechanism of CHF reduction caused by flow oscillation. It is commonly considered that critical heat flux condition in flow boiling is triggered by liquid film dryout in an annular two-phase flow regime at low mass fluxes, and by departure from nucleate boiling at high mass fluxes [8]. However, it is assumed in this work that boiling transition is caused by liquid film dryout, since this is the main mechanism under the thermal-hydraulic conditions encountered in boiling water reactors. It is considered that the critical heat fluxes in steady states can be used as a practically good basis to estimate the CHF value under an oscillatory condition. A simple theory is therefore developed to correlate the critical heat flux under a flow oscillation condition with those in steady states. Numerical simulations and experimental measurements of critical heat flux are conducted to test the validity of the proposed theory. Since liquid film dryout is regarded as the trigger mechanism for boiling transition in this work, a one-dimensional three-fluid model is used in the numerical simulation. The theory, numerical results and experimental results are described in the following three sections, respectively.

2. Fundamental concept

2.1. Dimensionless critical heat flux

If the duration of local liquid film dryout is short enough, a substantial rise in wall temperature can be avoided. However, to ensure the safety of boiling two-phase flow systems, the occurrence of local instantaneous liquid film dryout is regarded as the onset

* Corresponding author. Tel.: +81 6 6879 7257; fax: +81 6 6879 7247.
E-mail address: t-okawa@mech.eng.osaka-u.ac.jp (T. Okawa).

0017-9310/$ - see front matter © 2009 Elsevier Ltd. All rights reserved.
doi:10.1016/j.ijheatmasstransfer.2009.02.034

Nomenclature

a	model constant
a_i	interfacial area concentration (m^{-1})
C	mass concentration of droplets (kg/m^3)
C_d	drag coefficient
d	droplet diameter (m)
D	internal diameter of flow channel (m)
f_i	interfacial friction factor
f_w	wall friction factor
g	gravitational acceleration (m/s^2)
G	mass flux (kg/m^2s)
J	superficial velocity (m/s)
k_d	deposition mass transfer coefficient (m/s)
k_e	proportionality factor in the correlation for m_e (m/s)
L	heated length (m)
m_d	deposition rate of droplets (kg/m^2s)
m_e	entrainment rate of droplets (kg/m^2s)
M_i	interfacial drag force (N/m^3)
M_w	wall friction force (N/m^3)
N	total number of computational cells
P	pressure (Pa)
Pr	Prandtl number
q	critical heat flux (W/m^2s)
q_w	wall heat flux (W/m^2s)
Re	Reynolds number
t	time (s)
T	time period (s) or fluid temperature (K)
u	velocity (m/s)
u_{f0}	characteristic film velocity (m/s)
x	vapor quality
z	axial coordinate (m)
z_0	characteristic distance (m)

Greek symbols

α	volume fraction
δ	film thickness (m)
ΔG	amplitude of flow oscillation (kg/m^2s)
Δh_v	latent heat of vaporization (J/kg)
Γ	phase change rate (kg/m^3s)
μ	viscosity (Pa s)
π_e	dimensionless parameter to characterize m_e
ρ	density (kg/m^3)
σ	surface tension (N/m)

Superscript

$*$	dimensionless

Subscripts

AVE	average
d	droplet
EX	outlet
f	liquid film
IN	inlet
k	phase index
MAX	maximum
MIN	minimum
OSC	flow oscillation
v	vapor phase

of critical heat flux condition in this work. The situation encountered in a boiling channel under a flow oscillation condition is illustrated in Fig. 1. The channel wall is assumed to be uniformly heated, and sinusoidal periodic oscillation is applied to the inlet mass flux. Inlet mass flux G_{IN} is therefore expressed by

$$G_{IN} = G_{AVE} + \Delta G \sin\left(\frac{2\pi}{T_{OSC}} t\right) \tag{1}$$

where G_{AVE} is the time-averaged inlet mass flux, ΔG is the oscillation amplitude, T_{OSC} is the oscillation period and t is the time. For the sake of simplicity, it is assumed that the liquid and vapor phases are saturated, the heat capacity of the channel wall is negligibly small, and all the liquid moves as a liquid film in an annular two-phase flow regime. Under these assumptions, the vapor flow rate at an arbitrary axial location in the boiling channel may not vary significantly with time since all the heat applied to the channel wall is spent on liquid film vaporization. However, since the remaining liquid moves as a liquid film, the film flow rate would oscillate periodically due to the sinusoidal oscillation imposed on the inlet mass flux. If the wall heat flux is increased gradually, it is considered that instantaneous dryout of liquid film is first measured when the axial location corresponding to the minimum inlet flow rate $G_{MIN} = G_{AVE} - \Delta G$ arrives at the exit of the boiling channel. A notable difference caused by the flow oscillation would be the presence of a larger amount of liquid film around the axial location where the film flow rate is lowest (see Fig. 1). The present theory assumes that the mixing of liquid film in the axial direction is enhanced by the periodic axial distribution of the film flow rate produced by the flow oscillation. If no such mixing mechanism is available, the critical heat flux under the flow oscillation condition q_{OSC} may be equal to q_{MIN}, i.e., the critical heat flux in a steady state when the inlet mass flux is set to G_{MIN}. On the other hand, if the liquid film is completely mixed in the axial direction, the local maximum and local minimum of film flow rate delineated in Fig. 1 will disappear and the film flow rate will decrease monotonically toward the channel exit. In this case, q_{OSC} may be equal to q_{AVE}, i.e., the critical heat flux in a steady state when the inlet mass flux is equal to G_{AVE}. An appropriate scaling of q_{OSC} may therefore be given by

$$q^* = \frac{q_{OSC} - q_{MIN}}{q_{AVE} - q_{MIN}} \tag{2}$$

where q^* is the dimensionless critical heat flux under an oscillatory flow condition, and approaches zero and unity in the limiting cases of no mixing and complete mixing, respectively.

2.2. Dimensionless heated length

For the axial mixing of liquid film to take place, the thicker film region should interact with the minimum film thickness region corresponding to G_{MIN}. Since the migration velocity of liquid film u_f is dependent on the film thickness [9], inhomogeneous axial distribution of u_f is regarded as the primary cause of the axial mixing of the liquid film. A finite distance z_0 is necessary for a certain region to interact with the minimum film thickness region. Denoting the typical film velocities at the minimum film thickness region and the thicker film region by u_{f1} and u_{f2} ($u_{f1} < u_{f2}$, see Fig. 1), z_0 is proportional to the characteristic initial distance between the two regions $u_{f1}T_{OSC}/2$ and inversely proportional the dimensionless velocity difference $\Delta u_f/u_{f2}$, i.e., $z_0 = u_{f1}u_{f2}T_{OSC}/2\Delta u_f$; here, $\Delta u_f = u_{f2} - u_{f1}$. It can be confirmed that z_0 approaches its minimum value ($u_{f1}T_{OSC}/2$) for $u_{f2} \to \infty$ since $u_{f2}/\Delta u_f$ approaches unity, and z_0 approaches infinity for $\Delta u_f \to 0$. Since the heated length L should be longer than z_0 for the interaction to take place, the dimensionless heated length L^* may be defined by

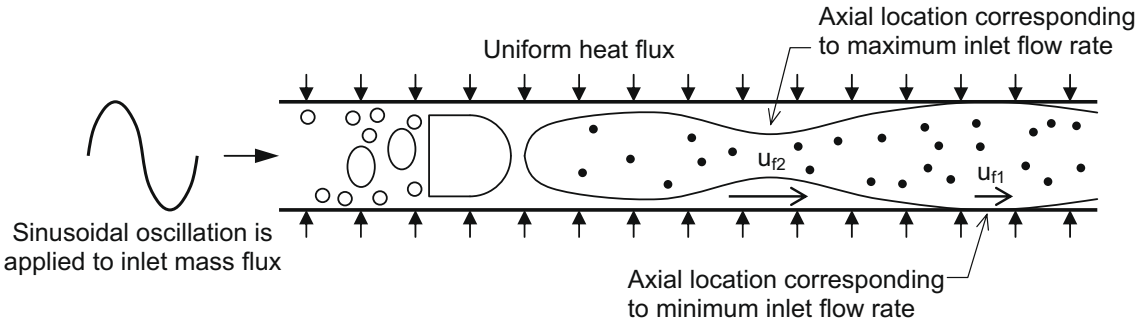

Fig. 1. Thermal-hydraulic condition supposed in a boiling channel under a flow oscillation condition.

$$L^* = \frac{L}{z_0} = \frac{2L}{u_{f0} T_{OSC}} \tag{3}$$

where the characteristic film velocity u_{f0} is defined by

$$u_{f0} = \frac{u_{f1} u_{f2}}{\Delta u_f} \tag{4}$$

From the present theory, it is considered that q^* moves from zero to unity with an increase in L^* since the axial mixing within the liquid film becomes noticeable with increased values of L^*. However, theoretical derivation of the functional relationship between q^* and L^* is difficult since the equations to determine the flow field inside the liquid film are highly nonlinear. Functions describing the relationship between q^* and L^* are therefore deduced using numerical and experimental results in the following sections. It should also be noted that several options are available in evaluating u_{f0} since the film velocity varies continuously in the axial direction in the actual thermal-hydraulic situations. The evaluation method of u_{f0} used in this work is described later in Section 3.3.

3. Film flow analysis

3.1. Governing equations and numerical methods

The computer program ANDRE [10] is used to calculate the critical heat flux under flow oscillation conditions. This program is based on the one-dimensional three-fluid model and uses the following continuity equations and momentum conservation equations as the basic equations:

$$\frac{\partial}{\partial t}(\alpha_k \rho_k) + \frac{\partial}{\partial z}(\alpha_k \rho_k u_k) = \sum_{p \neq k} (\Gamma_{pk} - \Gamma_{kp}) \tag{5}$$

$$\alpha_k \rho_k \frac{\partial u_k}{\partial t} + \alpha_k \rho_k u_k \frac{\partial u_k}{\partial z} = -\alpha_k \left(\frac{\partial P}{\partial z}\right) + M_{w,k} + M_{i,k} - \alpha_k \rho_k g + \sum_{p \neq k} \{\Gamma_{pk}(u_p - u_k)\} \tag{6}$$

where t is the time, z is the axial coordinate, α is the volume fraction, ρ is the density, u is the velocity, P is the pressure, M_w is the wall friction force, M_i is the interfacial drag force and g is the gravitational acceleration; the subscript k is the phase index (v: vapor, f: liquid film, d: droplets) and Γ_{pk} represents the phase change rate from phase p to phase k.

Constitutive equations are necessary to mathematically close basic Eqs. (5) and (6). The following relationship exists between the volume fractions:

$$\alpha_v + \alpha_f + \alpha_d = 1 \tag{7}$$

The wall friction force acting on the liquid film is calculated by

$$M_{w,f} = -\frac{2 f_w}{D} \rho_f |u_f| u_f \tag{8}$$

where D is the tube diameter. A simple correlation by Wallis [9] is used to evaluate the wall friction factor f_w:

$$f_w = \max\left(\frac{16}{Re_f}, 0.005\right) \tag{9}$$

where Re_f is the film Reynolds number ($=\alpha_f \rho_f u_f D/\mu_f$) and μ is the viscosity. Assuming that the channel wall is covered by a liquid film, the wall friction forces acting on the vapor phase and droplets are neglected. The interfacial drag force between the liquid film and vapor phase is expressed as

$$M_{i,f} = \frac{1}{2} f_i a_{i,f} \rho_v |u_v - u_f| (u_v - u_f) \tag{10}$$

where the interfacial area concentration $a_{i,f}$ is the function of α_f and the interfacial friction factor f_i are evaluated using the following correlation by Wallis [9]:

$$f_i = 0.005\left(1 + 300\frac{\delta}{D}\right) \tag{11}$$

The interfacial drag force between the droplets and vapor phase is calculated by

$$M_{i,d} = \frac{1}{8} C_d a_{i,d} \rho_v |u_v - u_d| (u_v - u_d) \tag{12}$$

where the interfacial area concentration $a_{i,d}$ is the function of α_d and the drop diameter d($a_{i,d} = 6\alpha_d/d$), and a correlation for a sphere by Clift and Gauvin [11] is used to evaluate the drag coefficient C_d:

$$C_d = \frac{24}{Re_d}(1 + 0.15 Re_d^{0.687}) + \frac{0.42}{1 + 42,500 Re_d^{-1.16}} \tag{13}$$

where Re_d is the droplet Reynolds number ($=\rho_v |u_v - u_f| d/\mu_v$) and d is assumed equal to 0.1 mm. From the principle of action and reaction, the interfacial drag force acting on the vapor phase can be calculated by $M_{i,v} = -M_{i,f} - M_{i,d}$.

Assuming that all the heat flux is spent for the phase change of liquid film to vapor, Γ_{fv} is calculated by $\Gamma_{fv} = q_w/\Delta h_v$; here, Δh_v is the latent heat of vaporization. The mass transfers between droplets and liquid film are evaluated using the correlations proposed by Okawa et al. [12]. The deposition rate of droplets m_d ($=\Gamma_{df} D/4$) is commonly expressed by

$$m_d = k_d C \tag{14}$$

where C is the mass concentration of droplets in the vapor core flow ($= \alpha_d \rho_d/(\alpha_v + \alpha_d)$). The following two correlations are used to calculate the deposition mass transfer coefficient k_d:

$$k_d \sqrt{\frac{\rho_v D}{\sigma}} = 0.0632\left(\frac{C}{\rho_v}\right)^{-0.5} \tag{15}$$

$$k_d = 0.009 \alpha_v u_v \left(\frac{C}{\rho_v}\right)^{-0.5} Re_v^{-0.2} Pr_v^{-2/3} \tag{16}$$

where σ is the surface tension, Re_v is the vapor phase Reynolds number ($=\alpha_v\rho_v u_v D/\mu_v$) and Pr is the Prandtl number. Eq. (15) is usually used to evaluate k_d, but Eq. (16) is used if P is lower than 0.5 MPa and the vapor quality x is higher than 0.25 (the ranges of $0.5 < P < 1$ MPa and $0.2 < x < 0.25$ are used for smooth transition between the two correlations). The entrainment rate of droplets m_e ($=\Gamma_{fd}D/4$) is expressed as

$$m_e = k_e \rho_f \pi_e^n \tag{17}$$

where π_e is a dimensionless parameter denoting the ratio of the interfacial shear force to the surface tension force acting on a liquid film ($\pi_e = f_i\rho_v(\alpha_v u_v)^2\delta/\sigma$). Depending on the range of π_e, different values are used for the proportionality factor k_e and the exponent n in Eq. (17): $k_e = 3.1\times10^{-2}$ m/s and $n = 2.3$ for $\pi_e < 0.0675$, $k_e = 1.6\times10^{-3}$ m/s and $n = 1.2$ for $0.0675 < \pi_e < 0.295$, and $k_e = 6.8\times10^{-4}$ m/s and $n = 0.5$ for $\pi_e > 0.295$. It is assumed that the deposition and entrainment of droplets take place in an annular two-phase flow regime. Hence, the mass transfer rates associated with the deposition and entrainment of droplets are evaluated using the above equations when α_v is greater than 0.75, and are neglected when it is smaller than 0.5; the range of $0.5 < \alpha_v < 0.75$ is used to increase m_d and m_e smoothly.

Since detailed descriptions of the numerical methods are found elsewhere [10], a brief outline only is given here. The governing equations are discretized on a staggered mesh using a semi-implicit scheme. Full donor cell differencing is used for the convection terms in continuity and momentum conservation Eqs. (5) and (6). The resulting algebraic nonlinear equations are solved numerically using the Newton–Raphson method. The tri-diagonal matrix for the pressure correction terms is derived using the Gauss–Jordan elimination method to find the inverse of the Jacobi matrix. The tri-diagonal matrix algorithm is used to solve the pressure correction equations.

3.2. Analytical conditions

In the initial condition, saturated water is injected from the bottom of a round tube at a constant mass flux G_{AVE}. The tube diameter and the heated length are denoted by D and L, respectively. Since adiabatic sections of L_A in length are placed at both ends of the heated section, the total tube length is equal to $L + 2L_A$. At the tube inlet, the relative velocities between the phases are neglected, and the volume fractions are set to $\alpha_f = 0.998$, $\alpha_d = 0.001$, and $\alpha_v = 0.001$. A constant pressure condition is applied to the tube outlet; the outlet pressure is denoted by P_{EX}. The gas and liquid phases are assumed saturated, and the thermal-hydraulic properties are evaluated at P_{EX}. After a steady state is established, sinusoidal oscillation is applied to the inlet mass flux G_{IN}; here, the oscillation period T_{OSC} is kept constant, and the oscillation amplitude is increased gradually to ΔG. When the amplitude reaches

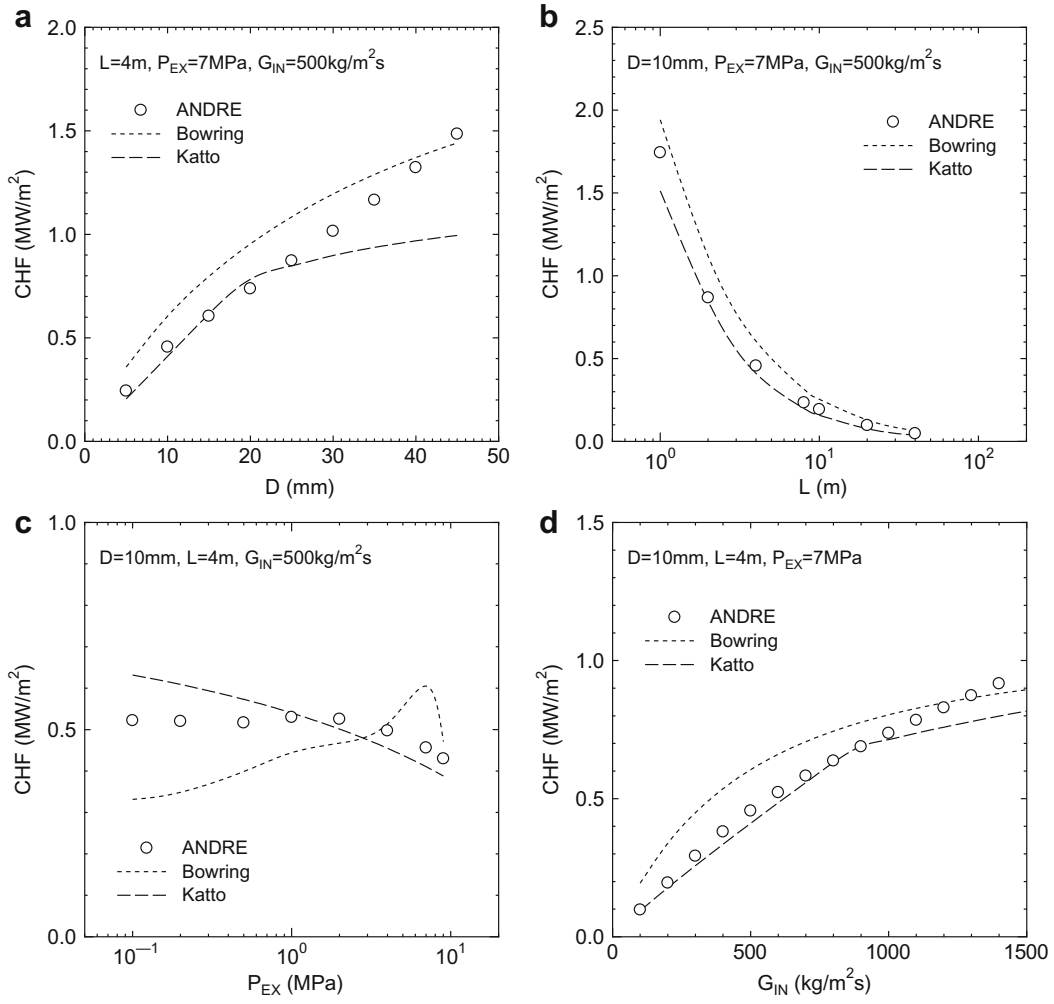

Fig. 2. Comparisons of CHFs calculated in steady states with those predicted by empirical correlations; dependences on (a) tube diameter, (b) heated length, (c) exit pressure, and (d) mass flux.

ΔG, uniform heat flux q_w applied within heated length L is increased gradually. The heat flux when the local value of α_f drops below 10^{-9} is regarded as the critical heat flux under the flow oscillation condition q_{OSC}.

In the reference condition, the analytical parameters are set as D = 10 mm, L = 4 m, P_{EX} = 7 MPa, G_{AVE} = 500 kg/m^{2}s, ΔG = 250 kg/m^{2}s (=0.5G_{AVE}), and T_{OSC} = 2.1 s. Keeping other parameters at the reference values, each parameter is varied individually within the ranges of D = 5–45 mm, L = 1–40 m, P_{EX} = 0.1–9 MPa, G_{AVE} = 100–2000 kg/m^{2}s, $\Delta G/G_{AVE}$ = 0.1–0.9, and T_{OSC} = 0.5–32 s. Since the calculated critical heat flux was not dependent on the total number of computational cells N significantly when N was within 50–200, the total tube length is equally divided into 100 computational cells. The time step is determined from the Courant number to avoid numerical instability.

3.3. Numerical results

To test the validity of the constitutive equations, the CHFs calculated in steady states are compared with those predicted using the correlations by Katto and Ohno [13] and by Bowring [14]. The results are shown in Fig. 2a–d. It can be confirmed that agreements of the CHFs calculated using ANDRE with those predicted using the empirical correlations are reasonably good to investigate the influence of flow oscillation on critical heat flux. However, since simple constitutive models were selected in the present work to highlight the influence of flow oscillation, agreements with the empirical correlations are not complete. For instance, dependence on G_{IN} is stronger in the simulation under the high mass flux condition as shown in Fig. 2d. Improvements of constitutive models for the droplet flow rate at the transition to annular flow and the film flow rate at the onset of critical heat flux condition are considered of particular importance to achieve better agreement since sufficient experimental information is not available on these quantities.

Fig. 3a displays the time variation of the axial distribution for the total mass flux G calculated under the reference condition; here, q_w is set to 0.24 MW/m^2, and the distributions at 10 time steps are depicted at intervals of 0.1T_{OSC}. It can be seen that G fluctuates within the range of $G_{AVE} \pm \Delta G$ at the inlet, but the fluctuation of G is mitigated noticeably at the outlet. The axial distributions of G_f, G_d and G_v are depicted in Fig. 3b–d, respectively. The three dashed lines in each figure indicate the distributions calculated in the steady states in which G_{IN} was set to G_{AVE} and $G_{AVE} \pm \Delta G$, respectively. Fig. 3b indicates that G_f at the exit is nearly zero when G_{IN} is set to $G_{AVE} - \Delta G$. Under the reference condition of oscillatory flow, however, the margin to the onset of liquid film dryout increases because of the reduction in the oscillation amplitude at the outlet. It is therefore expected from Fig. 3b that the critical heat flux calculated under the reference condition is lower than q_{AVE} but higher than q_{MIN}, which is consistent with the proposed theory (q^* is within 0–1). Fig. 3c and d, respectively show that the oscillation of G_d is also mitigated at the exit, and the distribution of G_v is not significantly influenced by the oscillation im-

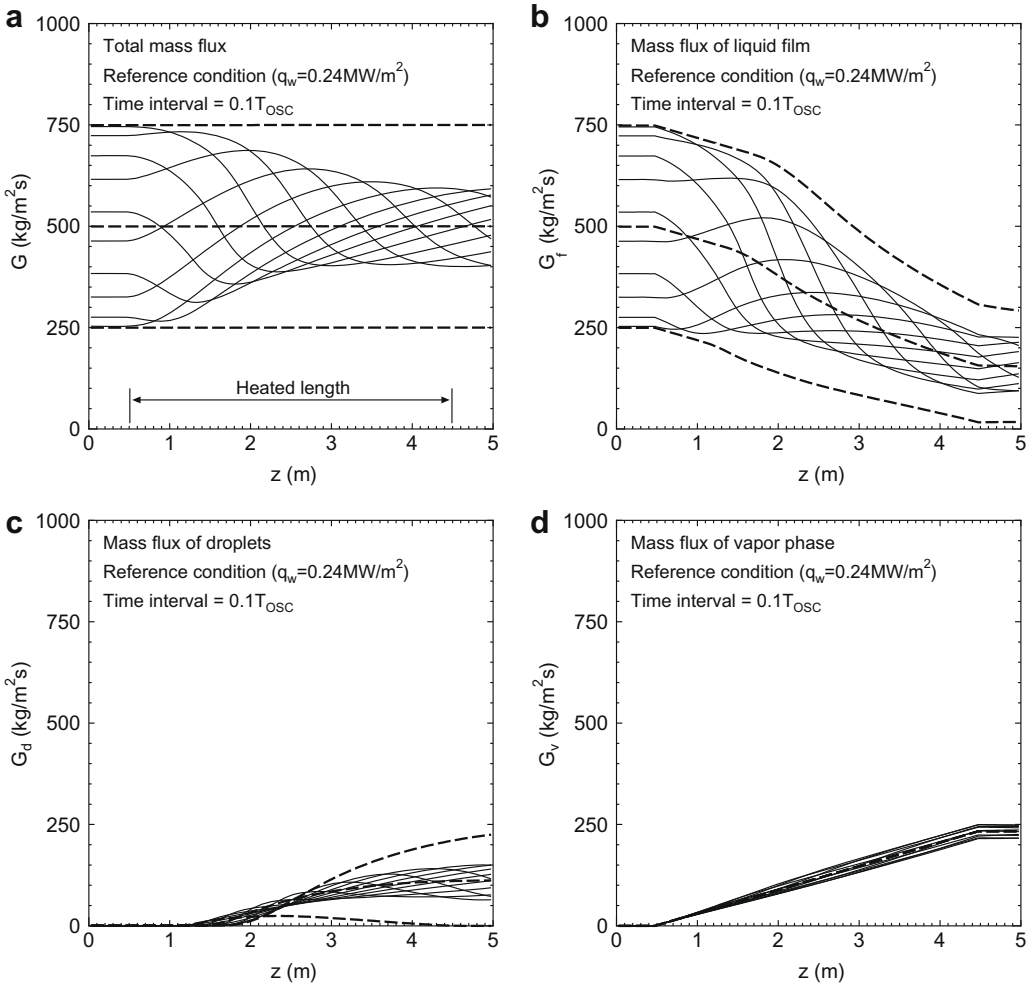

Fig. 3. Time variations of the axial mass flux distribution calculated under the reference condition: (a) all phases, (b) liquid film, (c) droplets, and (d) vapor phase.

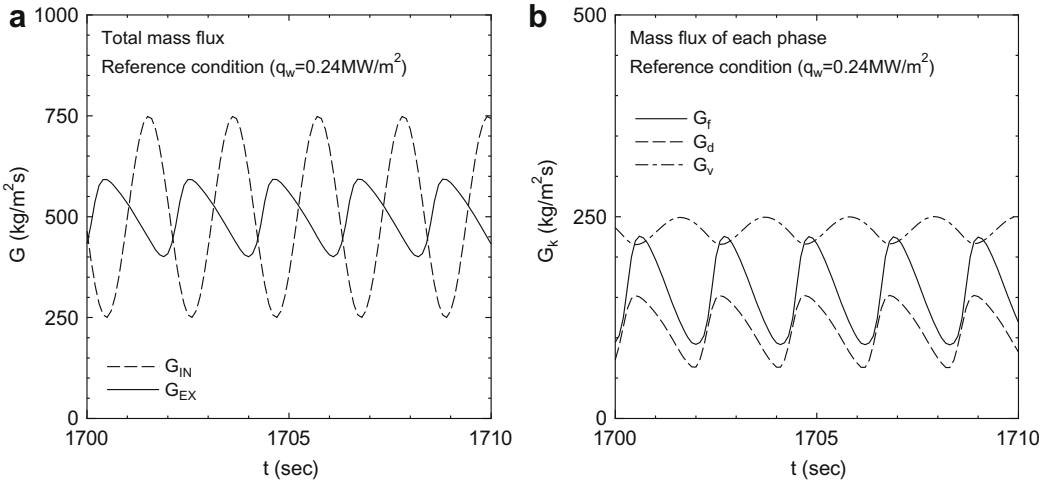

Fig. 4. Time variations of the mass fluxes: (a) total mass fluxes at the inlet and outlet, and (b) exit mass fluxes of liquid film, droplets and vapor phase.

posed on G_{IN}. The time variation of the total mass flux at the tube exit G_{EX} is depicted in Fig. 4a. The gradient is steeper downstream from the waves, which may be similar to the features of the breaking wave produced when the propagation speed is dependent on the transported variable [15]. Fig. 4b shows the time variation of the exit mass flux of each phase. It can be seen that the droplet flow rate G_d oscillates in nearly the same phase as the film flow rate G_f. This indicates that the local droplet flow rate is in rough proportion to the film flow rate. It was separately confirmed that the fluctuation of G is mitigated at the outlet as in Fig. 3a even when the droplet entrainment was neglected. It is therefore considered that the mitigation of the mass flux oscillation at the exit found in Fig. 3a can primarily be attributed to the axial liquid transport within the liquid film as supposed in the theory.

In Fig. 5a–f, the CHFs calculated under the oscillatory conditions q_{OSC} are compared with those in steady states; here, in the steady-state calculations, G_{IN} was set to G_{AVE} and G_{MIN} ($=G_{AVE} - \Delta G$). As supposed in the theory, the values of q_{OSC} are within the range of q_{MIN} to q_{AVE} in all the analytical conditions. It can be confirmed from Fig. 5b and f that q_{OSC} moves asymptotically from q_{MIN} to q_{AVE} with an increase in L and with a decrease in T_{OSC}. This is also consistent with the theory in which q^* is assumed to be an increasing function of $L^* = 2L/u_{f0}T_{OSC}$. Furthermore, u_{f0} generally decreases (L^* increases) with an increase in P_{EX} (reduction of vapor phase velocity), with an increase in ΔG (increase in Δu_f), and with a reduction of G_{AVE}. Consequently, q_{OSC} moves from q_{MIN} to q_{AVE} with increased values of P_{EX} and ΔG and with reduced value of G_{AVE} in Fig. 5c, e and d, respectively. On the other hand, L^* is not influenced significantly by D. Consequently, q_{OSC} always takes intermediate values between q_{MIN} and q_{AVE} in Fig. 5a.

The dependence of q^* on L^* is investigated quantitatively using the present numerical results. However, since the film velocity is not constant, several options are available in evaluating the characteristic film velocity u_{f0} defined by Eq. (4). For the sake of simplicity, the method shown below is used in this work. The balance of the interfacial shear force and the wall friction force acting on a liquid film is expressed by

$$\frac{1}{2}f_i\rho_v u_v^2 = \frac{1}{2}f_w\rho_f u_f^2 \tag{18}$$

Neglecting the dependence of f_i and f_w on thermal-hydraulic conditions, u_f is written by

$$u_f \propto \sqrt{\frac{\rho_v}{\rho_f}}J_v \tag{19}$$

Here, the volume fractions of liquid film and droplets are assumed to be sufficiently small ($u_v \approx J_v$). Supposing a limiting case in which almost all the liquid is evaporated, u_f is rewritten as

$$u_f \propto \frac{G_{AVE}}{\sqrt{\rho_f\rho_v}} \tag{20}$$

If the influence of ΔG is neglected, u_{f1} and u_{f2} in Eq. (4) may be roughly proportional to u_f calculated using the above equation. Fig. 6a shows the relationship between L^* and q^* when the film velocity calculated by Eq. (20) is used for u_{f0} as the first approximation. In spite of the simplifications made in evaluating u_{f0}, q^* is reasonably expressed as a monotonically increasing function of L^*. However, the effect of ΔG is not collapsed sufficiently, as expected. Since the velocity difference Δu_f increases with rising values of ΔG, it is expected that u_{f0} decreases with an increase in ΔG. To include the effect of ΔG, the following modification is therefore applied to u_{f0}:

$$u_{f0} = \frac{G_{AVE}}{\sqrt{\rho_f\rho_v}}\left(\frac{\Delta G}{G_{AVE}}\right)^n \tag{21}$$

Fig. 6b indicates that the effect of ΔG is collapsed fairly well if the value of the exponent n is set to -0.2 and that q^* is successfully correlated as a function of L^* in the form:

$$q^* = \tan h(aL^*) \tag{22}$$

where a is a model constant.

The validity of Eq. (22) is tested under extended analytical conditions in Fig. 7. Here, numerical simulations were performed for 810 cases, setting the analytical parameters as D = 5, 10, 20 mm, L = 2, 4, 8 m, P_{EX} = 1, 4, 7 MPa, G_{AVE} = 200, 500, 1000 kg/m^{2}s, $\Delta G/G_{AVE}$ = 0.1, 0.3, 0.5, 0.7, 0.9, and T_{OSC} = 2, 4 s. To save computation time, the total number of spatial meshes N was reduced to 50 in these calculations. Although q^* is slightly overestimated when the oscillation amplitude is large ($\Delta G/G_{AVE}$ = 0.9) and L^* is small, it can be confirmed that the critical heat flux under flow oscillation condition is satisfactorily correlated by Eq. (22) even under the extended conditions tested here.

4. Experiment

4.1. Experimental apparatus

A schematic diagram of the experimental apparatus is depicted in Fig. 8. Filtrated and deionized tap water was used as a working

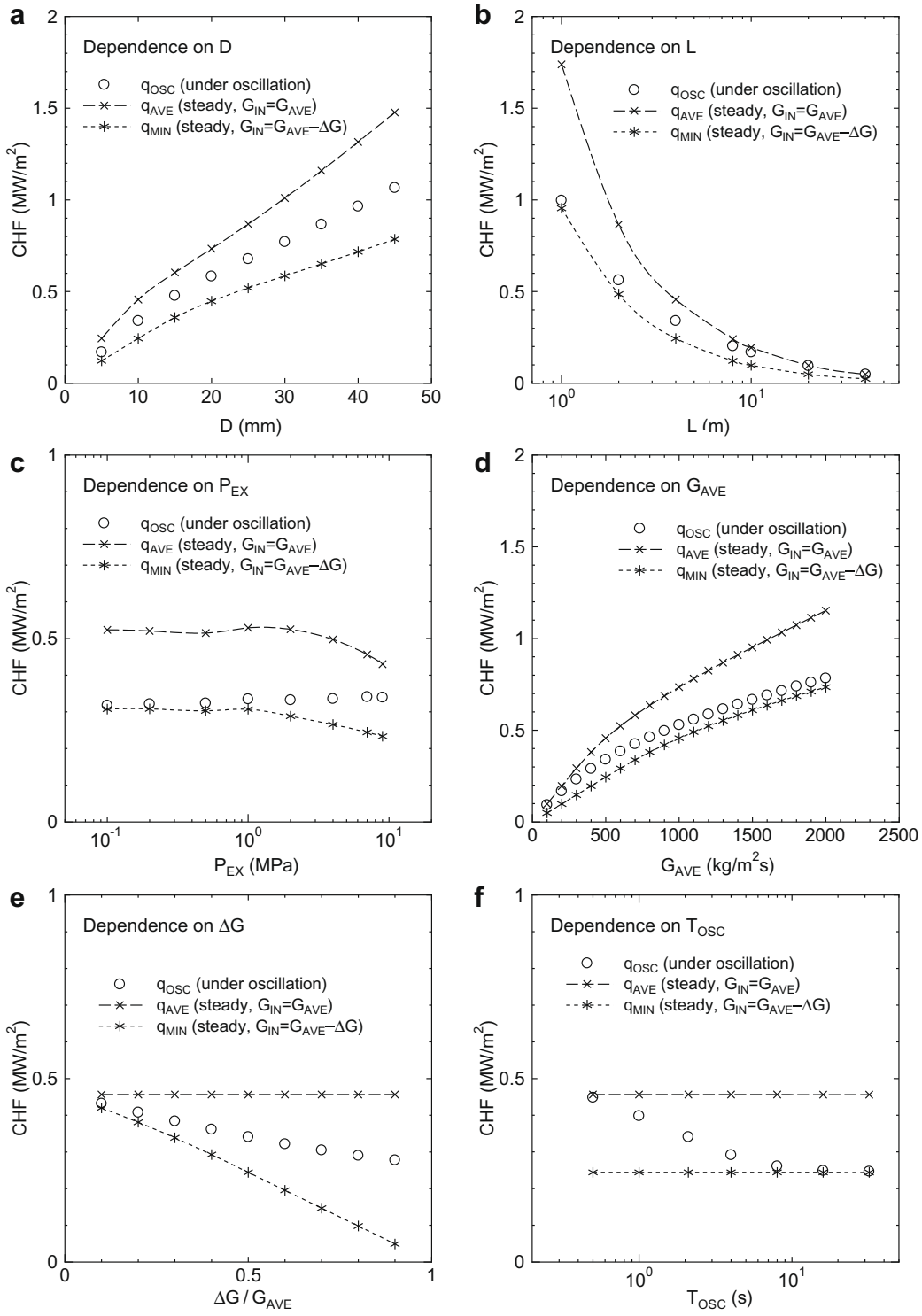

Fig. 5. Comparisons of CHFs calculated under oscillatory conditions with those in steady states; dependences on (a) tube diameter, (b) heated length, (c) exit pressure, (d) mean mass flux, (e) oscillation amplitude, and (f) oscillation period.

fluid, and was circulated using a multi-stage pump. Two needle valves and a turbine flow meter were used to control the inlet mass flux G_{IN}; the flow meter was accurate to within ±0.5%. The inlet flow rate was oscillated by changing the electric power applied to the circulation pump periodically. A 15-kW plug heater was used to raise and then maintain the water temperature at the inlet of the heated section T_{IN}. After exiting the pre-heating section, the water entered a vertical round tube of 12 mm in internal diameter and 0.8 mm in thickness made of SUS 316 stainless steel. A 60-kW DC power supply was used to heat the tube ohmically and generate steam-water annular flow inside it. The heated length, defined as the distance between the upper end of the lower electrode and the lower end of the upper electrode, was 1360 mm. The copper electrodes were covered with rubber sheets for thermal insulation. The top of the vertical test section was connected with the upper tank (which was open to atmosphere) in order to separate the

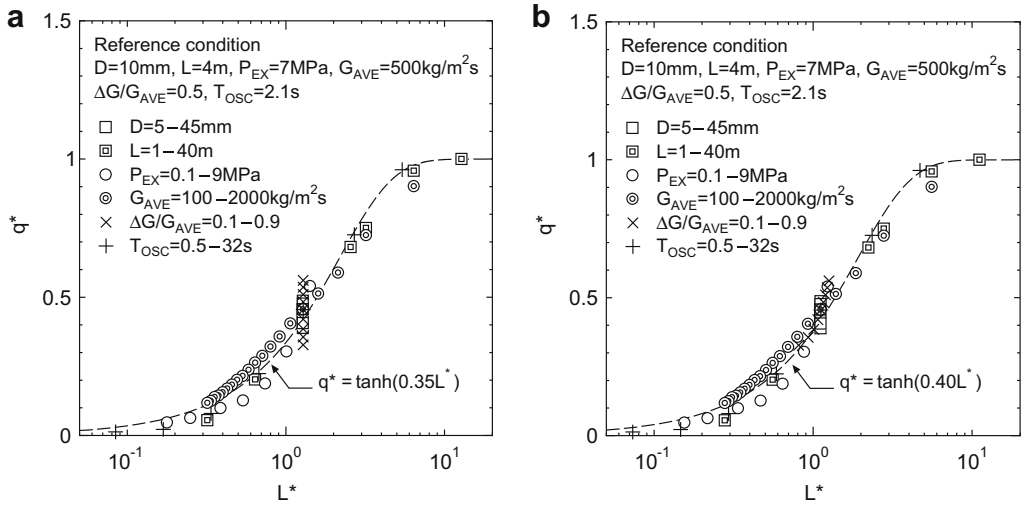

Fig. 6. Relationships between L^* and q^* obtained in the numerical simulations; the exponent n in Eq. (21) is set to (a) 0, and (b) −0.2.

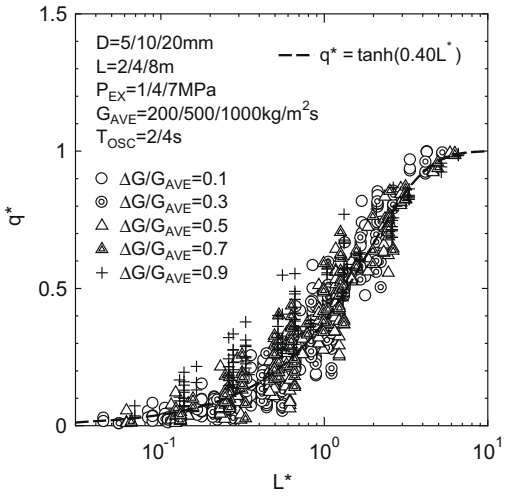

Fig. 7. Relationships between L^* and q^* obtained in extended analytical conditions.

vapor phase from the liquid phase. The liquid phase was then returned to the circulation pump, while the vapor phase was condensed in the separator or released into the atmosphere.

The fluid temperature was measured at the inlet and outlet of the preheating section with type-K thermocouples accurate to within ±1.5 K. Pressure transducers accurate to within ±7.5 kPa were used to measure the pressures at the inlet and outlet of the heated section. The heat flux applied to the fluid was calculated from the electric current passing through the heated section and the electrical resistance of the tube material. Ten type-K thermocouples were spot-welded to the outer surface of the heated section to measure wall temperatures. Initiation of the boiling transition was expected to occur at the exit of heated section since the channel wall was heated uniformly. Four thermocouples were therefore placed as the BT (boiling transition) detectors near the exit of the heated section to detect the transition to critical heat flux condition without fault. The heated section was not thermally insulated, but heat loss to the ambient air was estimated as less than 1 kW/m^2 from calculation using the heat transfer equation proposed by Churchill and Chu [16]. Experimental data were recorded every 1 ms using a data acquisition system.

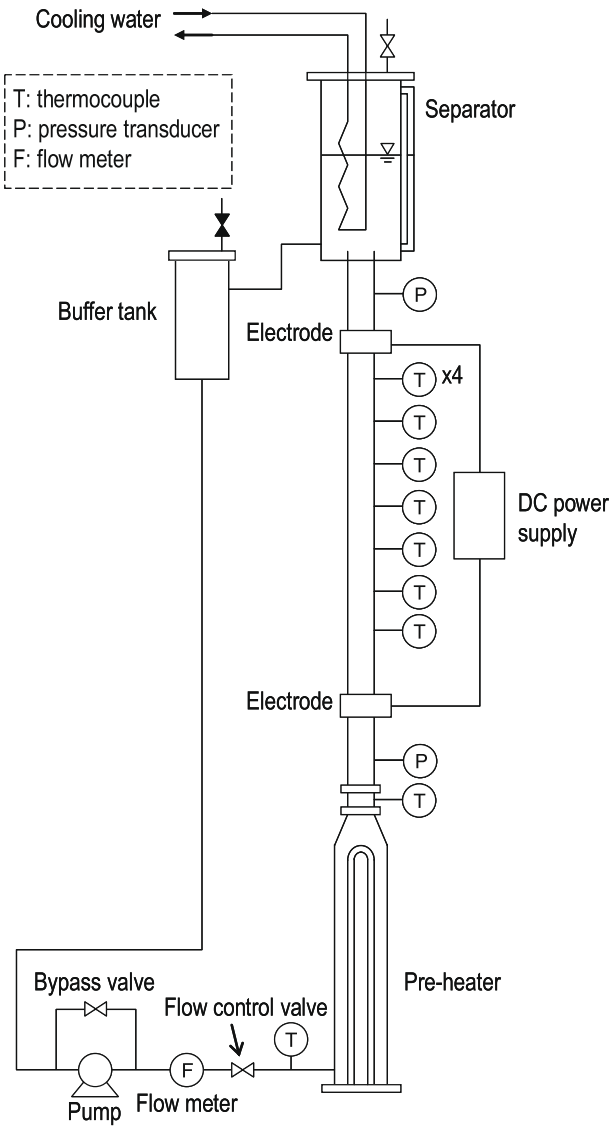

Fig. 8. Schematic diagram of experimental apparatus.

4.2. Experimental conditions

The critical heat fluxes were measured under 8 steady states and 34 flow oscillation conditions. The time-averaged liquid temperature at the inlet T_{IN} was set to 374 ± 2 K in all the experiments. In the steady-state experiments, G_{IN} was set to 12–189 kg/m^{2}s. The upper limit of G_{IN} was determined from the maximum power output of the DC power supply. In the flow oscillation conditions, the ranges of G_{AVE} and $\Delta G/G_{AVE}$ were within 41–237 kg/m^{2}s and 0.25–0.84, respectively, and the oscillation period T_{OSC} was set to 2, 5, 10 and 20 s.

Fig. 9a and b show the typical time transients of the wall temperatures T_W and the inlet mass flux G_{IN} measured when critical heat flux condition was reached; here, $T_{W,BT}$ denotes the wall temperatures measured by the BT detectors, and Fig. 9a and b indicate the results obtained under steady and oscillatory conditions, respectively. In the flow oscillation conditions, the characteristic temperature rise was measured by the BT detectors periodically as shown in Fig. 9b since instantaneous liquid film dryout and subsequent rewetting of the heated surface were repeated near the exit of the heated section. In the present work, the wall heat flux at which the amplitude of the characteristic temperature rise exceeded 5 K was regarded as the critical heat flux. The critical heat flux in the steady state was determined using the same method for consistency (see Fig. 9a). Because of the finite heat capacity of the channel wall, the inner surface of the heated wall should be kept dry for a certain time period Δt for the transition to critical heat flux condition to be detected using the present method. From the results of numerical calculations using the heat conduction equation, Δt was estimated to within 10% of T_{OSC}. Since Δt was reasonably shorter than T_{OSC}, it was assumed that the measured critical heat flux was not significantly influenced by the heat capacity of the channel wall.

4.3. Experimental results

The critical heat fluxes measured in the steady states are compared with those predicted using the generalized correlation by Katto and Ohno [13] and the empirical correlation by Bowring [14] in Fig. 10. It can be seen that the present data are in good agreement with the correlation by Bowring that was developed solely for the forced convective flow of water. To investigate the relationship between critical heat fluxes under steady states and those under oscillatory conditions, the critical heat fluxes obtained in the steady states were approximated using two second-order polynomials. The resulting fitting curve is indicated by the solid line in Fig. 10.

Typical experimental data of q_{OSC} measured under flow oscillation conditions are plotted against G_{AVE}, $\Delta G/G_{AVE}$ and T_{OSC} in Fig. 11a–c, respectively. It can be seen that q_{OSC} is generally smaller than the value measured in the steady state q_{AVE}, and that the deviation from q_{AVE} becomes significant with increased values of G_{AVE}, $\Delta G/G_{AVE}$ and T_{OSC}. As demonstrated in Figs. 6 and 7, in the numerical simulations, q_{OSC} was expressed fairly well by

$$q_{OSC} = q_{AVE} - [1 - \tanh(aL^*)](q_{AVE} - q_{MIN}) \quad (23)$$

Since increases in G_{AVE} and T_{OSC} lead to the reduction of L^* (see Eqs. (3) and (21)) and increases in $\Delta G/G_{AVE}$ result in the reduction of q_{MIN}, the influences of these parameters on the experimental values of q_{OSC} relative to q_{AVE} shown in Fig. 11 are in qualitative agreement with the numerical results.

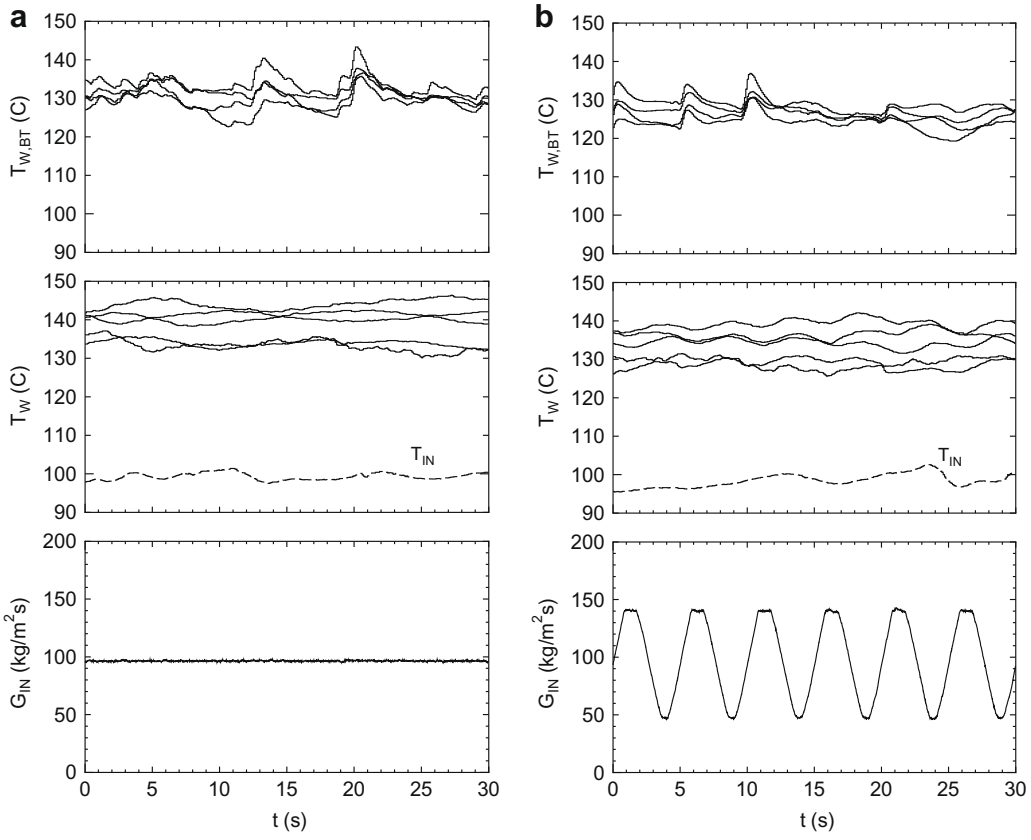

Fig. 9. Typical time transients of wall temperatures and inlet mass flux when the critical heat flux condition is reached; results obtained under (a) steady state (P_{EX} = 142 kPa, T_{IN} = 373 K, G_{IN} = 96 kg/m^{2}s, q_W = 346 kW/m^2), and (b) flow oscillation condition (P_{EX} = 137 kPa, T_{IN} = 372 K, G_{AVE} = 97 kg/m^{2}s, $\Delta G/G_{AVE}$ = 0.48, T_{OSC} = 5 s, q_W = 255 kW/m^2).

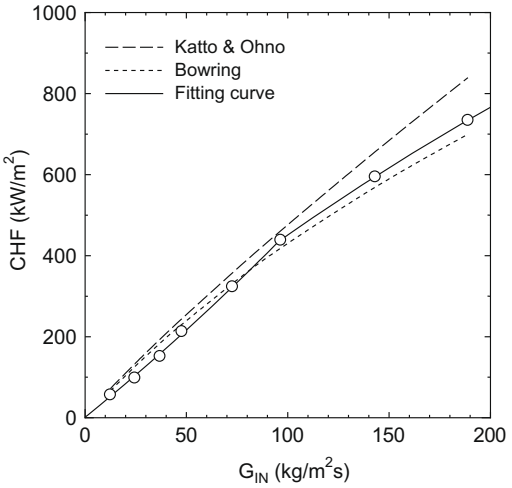

Fig. 10. Critical heat fluxes measured in the steady states.

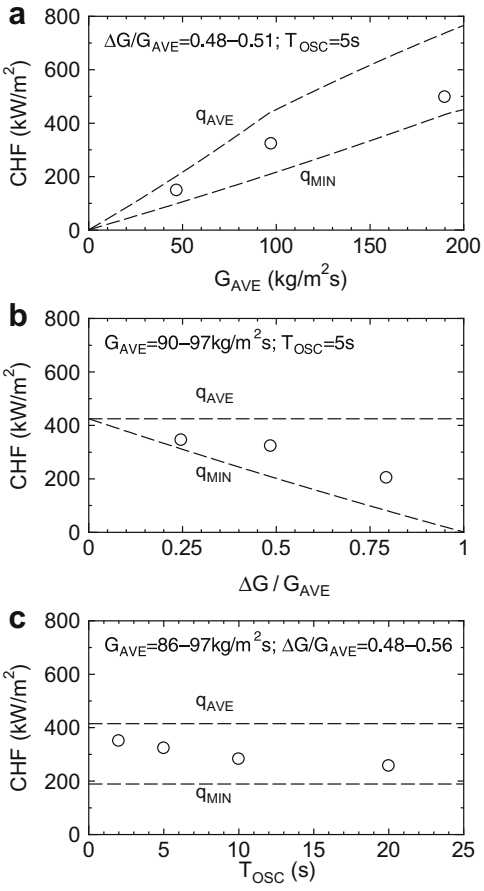

Fig. 11. Typical critical heat flux data measured under flow oscillation conditions; dependences on (a) mean mass flux, (b) oscillation amplitude, and (c) oscillation period.

Fig. 12 displays all the experimental data for dimensionless critical heat flux measured in oscillatory conditions. It can be confirmed that q^* decreases with an increase in T_{OSC} if both G_{AVE} and ΔG are in the same range, which agrees with the numerical results. However, the dependence of q^* on $\Delta G/G_{AVE}$ is not consistent with the numerical results. In the numerical simulations, q^* increased with rising values of $\Delta G/G_{AVE}$. Consequently, q^* correlated reasonably well as a function of L^* if the influence of $\Delta G/G_{AVE}$ was included using Eq. (21). However, in the experimental results shown in Fig. 12, no definite correlation can be seen between $\Delta G/G_{AVE}$ and q^*.

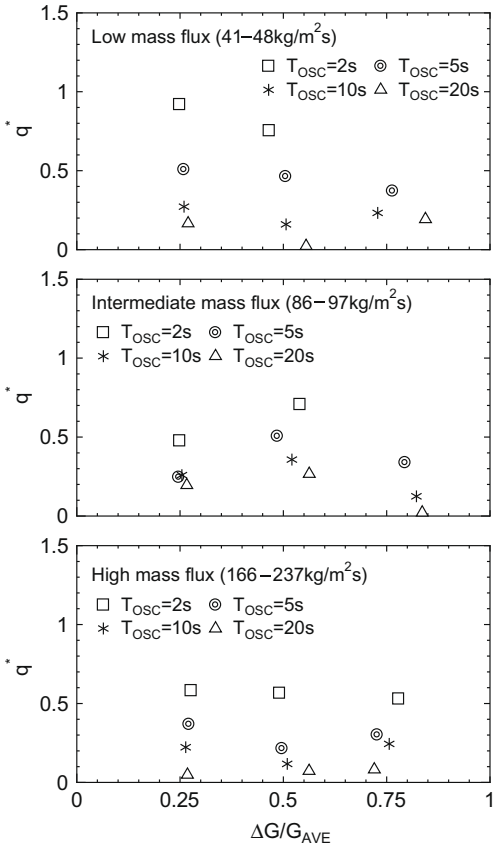

Fig. 12. Dimensionless critical heat fluxes measured under flow oscillation conditions.

The experimental data of q^* are plotted against L^* in Fig. 13; here, since no clear dependence of q^* on $\Delta G/G_{AVE}$ was found in Fig. 12, the exponent n in Eq. (21) is set to 0 and −0.2 in Fig. 13a and b, respectively. As an overall trend, q^* increases with rising values of L^*, indicating that L^* and q^* are a promising set of scaling parameters to characterize the critical heat flux under flow oscillation conditions. However, regardless of the value of n, the experimental values of q^* are much greater than the correlating line of the numerical results. The deviation from the correlating line becomes more significant with increases in G_{AVE}. It is suspected that this discrepancy was partly caused by experimental constraints. For instance, as shown in Fig. 9b, the inlet mass flux did not follow the sine curve exactly and the inlet temperature fluctuated slightly in the experiments. It is, however, known that the surface of liquid film in annular flow is commonly covered with complex interfacial waves such as ripple and disturbance waves. In particular, disturbance waves that occur at high liquid flow rates have a height several times the mean film thickness, move at a velocity greater than the mean film velocity, and retain their identity throughout the flow channel [17–19]. It is therefore considered highly possible that disturbance waves contributed to the axial liquid transport in the present experiments. Since the effect of the disturbance waves was not included in the numerical simulations, the discrepancy between the numerical and experimental results seen in Fig. 13 may be attributed to the axial mixing of liquid film caused by the disturbance waves.

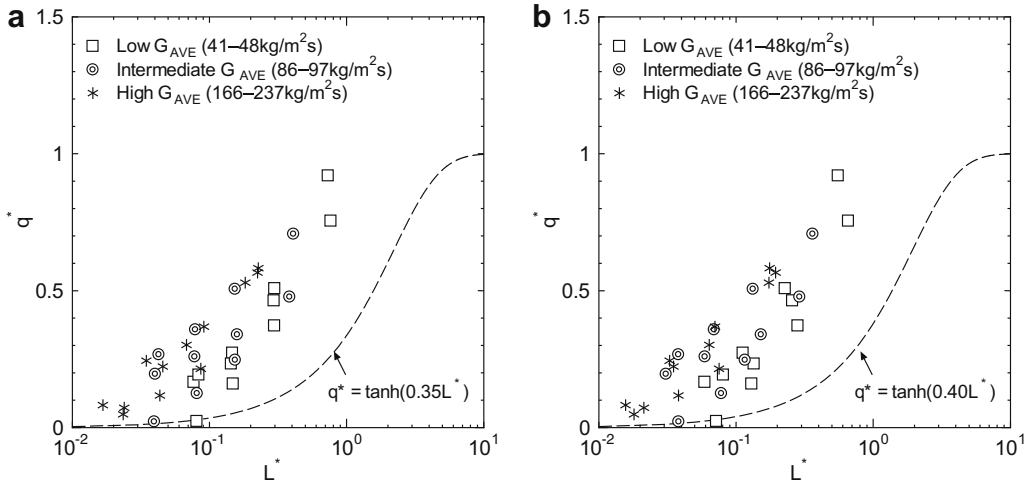

Fig. 13. Relationships between L^* and q^* obtained in the experiments; the exponent n in Eq. (21) is set to (a) 0, and (b) −0.2.

5. Summary and conclusions

The effect of sinusoidal oscillation of the inlet mass flux on the critical heat flux in forced convective flow was investigated. It was assumed that boiling transition is induced by liquid film dryout in an annular two-phase flow regime since it is the main trigger mechanism for boiling transition encountered in boiling water reactors. It is considered that the critical heat flux in a steady state can be used as a practical basis to estimate the critical heat flux under an oscillatory condition. A simple theory was therefore developed to link the critical heat flux under a flow oscillation condition to those in the steady states. The proposed theory assumes that the upper and lower limits of CHF under a flow oscillation condition are given by the CHFs in steady states in which the inlet mass flux is equal to the time-averaged and minimum values, respectively. The critical heat flux under an oscillatory condition was normalized based on this concept. It was further assumed that the reduction of CHF caused by flow oscillation is mitigated by the axial liquid transport within the liquid film. This assumption led to the introduction of the dimensionless heated length as a promising parameter to characterize the dimensionless critical heat flux under a flow oscillation condition. A simple method to evaluate the dimensionless heated length was also developed.

To test the validity of the present theory and find the functional relationship between the two dimensionless parameters, numerical simulations using a one-dimensional three-fluid model and experimental measurements of critical heat flux under atmospheric pressure were carried out. It was shown that the dimensionless heated length collapses the dimensionless critical heat flux reasonably well in both approaches, which demonstrated the validity of the proposed theory. However, the dimensionless critical heat flux was generally higher in the experiment than in the numerical simulation, indicating that the present numerical model evaluates the effect of flow oscillation conservatively. Although the main reason for the discrepancy between the numerical and experimental results was not identified, it is suggested that disturbance waves forming on the surface of the liquid film might have contributed to enhancing the axial mixing of the liquid film in the experiments.

Acknowledgements

The authors express their gratitude to A. Hotta, K. Nozaki (TEPSYS), Y. Takeuchi and Y. Yamamoto (TOSHIBA) for their roles in productive discussions related to this study. This work was partly carried out within the task "Research on Hyper ABWR Plants of Extended Core Power Density" entrusted by the Ministry of Economy, Trade and Industry of Japan.

References

[1] M. Aoyama, K. Haikawa, L.E. Fennern, R. Yoshioka, T. Ohta, T. Anegawa, Optimization of core design for the next generation BWR, in: Proceedings of the 5th International Conference on Nuclear Engineering, Nice, France, 1997, Paper No. ICONE5-2636.
[2] M. Chaki, M. Murase, Evaluation of the sensitivity of a two-phase flow model for steam separators analysis, in: Proceedings of the 14th International Conference on Nuclear Engineering, Miami, Florida, 2006, Paper No. ICONE14-89507.
[3] J.G.M. Andersen, J.L. Casillas, B.S. Shiralkar, Application of advanced thermal hydraulic TRACG model to preserve operating margins in BWRs at extended power uprate conditions, in: Proceedings of the International Congress on Advances in Nuclear Power Plants, Reno, Nevada, 2006, pp. 1066–1077.
[4] K. Arai, A. Murase, R. Hamazaki, M. Kuroki, AB1600-progress of ABWR technology toward next generation ABWR, Nuclear Eng. Des. 238 (2008) 1902–1908.
[5] M. Ozawa, M. Hirayama, H. Umekawa, Critical heat flux condition induced by flow instabilities in boiling channels, Chem. Eng. Technol. 25 (2002) 1197–1201.
[6] M. Ozawa, H. Umekawa, Y. Yoshioka, A. Tomiyama, Dryout under oscillatory flow condition in vertical and horizontal tubes – experiments at low velocity and pressure conditions, Int. J. Heat Mass Transfer 36 (1993) 4076–4078.
[7] H. Umekawa, M. Ozawa, T. Mitsunaga, K. Mishima, T. Hibiki, Y. Saito, Scaling parameters of CHF under oscillatory flow conditions, Heat Transfer – Asian Res. 28 (1999) 541–550.
[8] J.G. Collier, J.R. Thome, Convective Boiling and Condensation, third ed., Oxford University Press, Oxford, 1994. pp. 325–374.
[9] G.B. Wallis, One-dimensional Two-phase Flow, McGraw-Hill, New York, 1969. pp. 315–374.
[10] T. Okawa, T. Kitahara, K. Yoshida, T. Matsumoto, I. Kataoka, New entrainment rate correlation in annular two-phase flow applicable to wide range of flow condition, Int. J. Heat Mass Transfer 45 (2002) 87–98.
[11] R. Clift, J.R. Grace, M.E. Weber, Bubbles Drops and Particles, Academic Press, New York, 1978. pp. 97–141.
[12] T. Okawa, A. Kotani, I. Kataoka, Masanori Naito, Prediction of the critical heat flux in annular regime in various vertical channels, Nuclear Eng. Des. 229 (2004) 223–236.
[13] Y. Katto, H. Ohno, An improved version of the generalized correlation of critical heat flux for the forced convective boiling in uniformly heated vertical tubes, Int. J. Heat Mass Transfer 27 (1984) 1641–1648.
[14] R.W. Bowring, A simple but accurate round tube uniform heat flux dryout correlation over the pressure range 0.7–17 MN/m^2, AEEW-R789, 1972.
[15] G.B. Whitham, Linear and Nonlinear Waves, John Wiley & Sons, New York, 1974. pp. 19–67.
[16] S.W. Churchill, H.H.S. Chu, Correlating equations for laminar and turbulent free convection from a vertical plate, Int. J. Heat Mass Transfer 18 (1975) 1323–1329.
[17] N.S. Hall-Taylor, R.M. Nedderman, The coalescence of disturbance waves in annular two phase flow, Chem. Eng. Sci. 23 (1968) 551–564.
[18] G.F. Hewitt, N.S. Hall-Taylor, Annular Two-phase Flow, Pergamon Press, Oxford, 1970. pp. 98–126.
[19] B.J. Azzopardi, Drops in annular two-phase flow, Int. J. Multiphase Flow 23 (1997) 1–53.